JACS Au
AN OPEN ACCESS JOURNAL OF THE AMERICAN CHEMICAL SOCIETY

pubs.acs.org/jacsau

Article

Sequence-Activated Fluorescent Nanotheranostics for Real-Time Profiling Pancreatic Cancer

Yining Tao,[‖] Chenxu Yan,[‖] Dan Li, Jianfeng Dai, Yingsheng Cheng, Hui Li,* Wei-Hong Zhu, and Zhiqian Guo*

Cite This: *JACS Au* 2022, 2, 246–257

Read Online

ACCESS | Metrics & More | Article Recommendations | Supporting Information

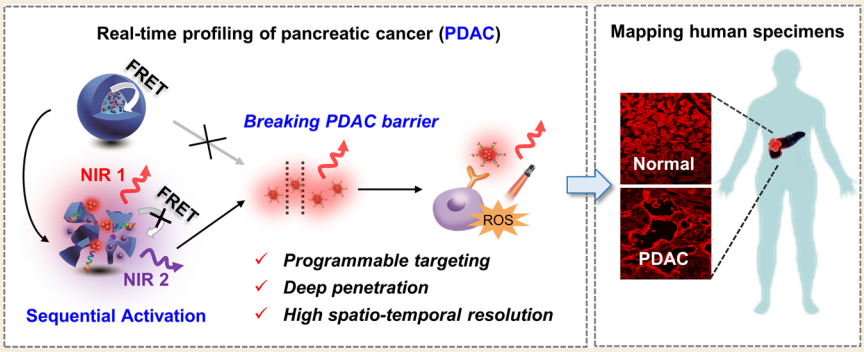

ABSTRACT: Pancreatic ductal adenocarcinoma (PDAC), as one of the most malignant tumors with dense desmoplastic stroma, forms a specific matrix barrier to hinder effective diagnosis and therapy. To date, a paramount challenge is in the search for intelligent nanotheranostics for such hypopermeable tumors, especially in breaking the PDAC-specific physical barrier. The unpredictable *in vivo* behaviors of nanotheranostics, that is, real-time tracking where, when, and how they cross the physical barriers and are taken up by tumor cells, are the major bottleneck. Herein, we elaborately design sequence-activated nanotheranostic TCM-U11&Cy@P with dual-channel near-infrared fluorescence outputs for monitoring *in vivo* behaviors in a sequential fashion. This nanotheranostic with a programmable targeting capability effectively breaks through the PDAC barriers. Ultimately, the released aggregation-induced emission (AIE) particle TCM-U11 directly interacts with PDAC cells and penetrates into the deep tissue. Impressively, this fluorescent nanotheranostic intraoperatively can map human clinical PDAC specimens with high resolution. We believe that this unique sequence-activated fluorescent strategy expands the repertoire of nanotheranostics in the treatment of hypopermeable tumors.

KEYWORDS: *near-infrared fluorescence, aggregation-induced emission, pancreatic ductal adenocarcinoma, sequence-activated, nanotheranostics*

INTRODUCTION

Poorly permeable tumors, with the unique stroma-rich microenvironment, severely limit the site-specific bioavailability of nanotheranostics, preventing the achievement of clinical efficacy.[1−4] For example, pancreatic ductal adenocarcinoma (PDAC) is an extremely malignant tumor with a high fatality rate and reported an overall five-year survival rate of less than 10%.[5,6] Unfortunately, PDAC is extremely difficult to diagnose due to its hidden location, lack of specific symptoms, and aggressive behavior.[7,8] Most current strategies for incremental improvements to such solid tumors merely rely on the enhanced permeability and retention (EPR) effect or active targeting ligands.[9−11] However, the natural protective physical barrier from a dense desmoplastic stroma becomes a major obstacle for the effective diagnosis and treatment of PDAC, thereby hindering deep and uniform penetration of nanotheranostics.[12−14] Even with the incorporation of active targeting moieties, cellular uptake in PDAC deep tissues still faces the substantial barrier of nanoparticle internalization only within the first few layers of tumor cells (proximal to the vasculature).[15−17] To date, a paramount challenge is in the search for intelligent nanotheranostics for such hypopermeable tumors, especially in breaking the PDAC-specific physical barrier.

Toward this goal, the programmable-responsive strategy that tunes their properties (e.g., regulating particle size, exposing

Received: December 13, 2021
Published: January 10, 2022

ACS Publications

© 2022 The Authors. Published by American Chemical Society

https://doi.org/10.1021/jacsau.1c00553
JACS Au 2022, 2, 246–257

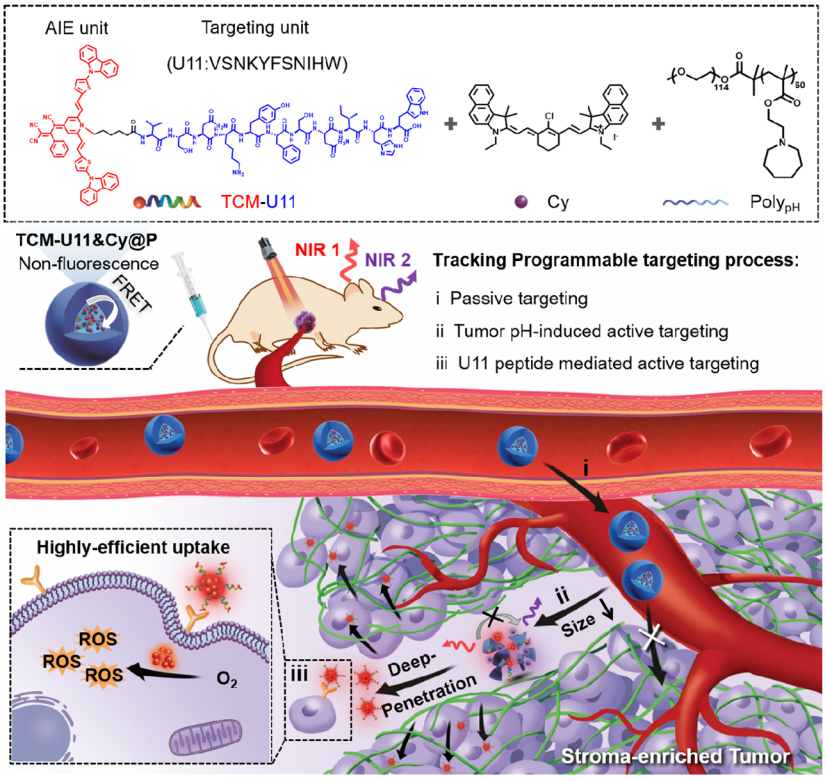

Figure 1. Schematic illustration of sequence-activated fluorescent nanotheranostics for programmable targeting of the pancreatic tumor. (i) Owing to the passive tumor targeting, TCM-U11&Cy@P with an initially large particle size is delivered to tumor tissue via the enhanced penetration and retention (EPR) effect. (ii) In an acidic tumor microenvironment, TCM-U11&Cy@P executes micelle dissociation, followed by the release of the Cy (emission at 830 nm) and TCM-U11 particles (broad emission at 650 nm). Owing to this tumor microenvironment-triggered size transformation, the resulting small AIE particles could be further delivered into the deep PDAC tissue, and the fluorescence enhancement at 650 nm could track the pathways in which the stimuli-induced particle change occurs. (iii) Then, the surface-grafted U11 peptides of TCM-U11 particles target to the receptors (uPAR) overexpressed on PDAC cells in the deep tissue and thereby facilitate deep PDT to ablate the tumor.

active targeting ligand, etc.)[18−22] in response to environmental stimuli would realize robust and effective delivery to deep PDAC tissue.[23−25] In particular, it is still a critical challenge to reveal the *in vivo* behavior of these nanotheranostics, that is, real-time tracking where, when, and how they cross the PDAC barriers and are taken up by tumor cells. For instance, the size of nanoparticles could be tailored for purposes of improving tumor permeability for PDAC, but still little is known about the real-time pathways in which the stimuli-induced particle change occurs.[26−28] Specifically, toward breaking the PDAC-specific matrix barrier, such nanotheranostics require monitoring multistaged *in vivo* behaviors in a sequential fashion and synergistically *in situ* initiating intratumoral therapy. Inspired by the Boolean logic idea,[29−32] we envisioned that the integration of interactional fluorophores with activatable dual-emission into nanotheranostics is the key strategy to solve this dilemma, which would greatly expand the repertoire of programmable-responsive nanotheranostics in the treatment of hypopermeable tumors.

Herein, we innovatively present a programmable targeting strategy of sequence-activated fluorescent nanotheranostics for effectively crossing the PDAC-specific matrix barrier, wherein all of these sequential *in vivo* behaviors are monitored via activatable dual-channel near-infrared (NIR) fluorescence to enhance tumor permeability and therapeutic efficacy. As illustrated in Figure 1, this fluorescent nanotheranostic (named TCM-U11&Cy@P) contains three components: the diblock copolymer serving as the carrier with ultrasensitive response to pH, AIEgen TCM-DN (FRET donor) covalently attached with U11 peptide (TCM-U11) for targeting PDAC cells, and the cyanine fluorophore (Cy) as an NIR Förster resonance energy transfer (FRET) acceptor. First of all, TCM-U11&Cy@P remains nonemissive and maintains a relatively large particle size at the normal pH of 7.4. After being delivered reaching the tumor site through passive tumor targeting (EPR effect), TCM-U11&Cy@P dissociates under pH <6.8, along with the release of the Cy (fluorescence enhancement at 830 nm) and small AIEgen nanoparticles (size <50 nm). Owing to the pH-triggered size transformation by the acidic tumor microenvironment, the resulting small AIE nanoparticles could further penetrate into the deep PDAC tissue, and thus, the fluorescence enhancement at 650 nm could real-time monitor the pathways in which the stimuli-induced particle size change occurs. Then, the surface-grafted U11 peptides of AIE nanoparticles are directly exposed and thereby bind to receptors (uPAR) overexpressed on PDAC cells, markedly facilitating cellular internalization and remarkable reactive oxygen species generation for photodynamic therapy (PDT) in living mice. Notably, this programmable targeting strategy offers unique capabilities in dual-channel monitoring *in vivo* physiological processes, thereby making a breakthrough of inherent PDAC-specific physical barriers. Notably, the efficiently enhanced intratumoral distribution of this nanotheranostic allows for intraoperatively mapping clinical specimens with high resolution. This unique sequence-activated fluorescent nanotheranostic would pave a

https://doi.org/10.1021/jacsau.1c00553
JACS Au 2022, 2, 246−257

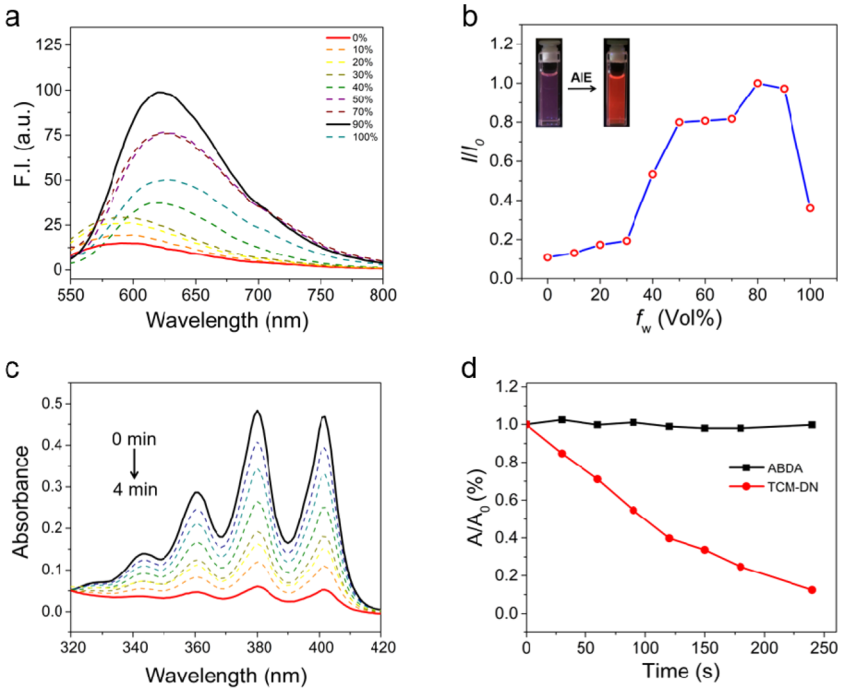

Figure 2. Spectral properties of the significant AIE performance and photodynamic effect of TCM-DN. (a) Fluorescence emission spectra of TCM-DN (10^{-5} M) in DMSO/water mixtures with different volume fractions of water (f_w), λ_{ex} = 510 nm. (b) I/I_0 plots of TCM-DN in a mixture of DMSO/water, where I is the fluorescence intensity at 650 nm, and I_0 is the fluorescence intensity of TCM-DN in 80% water, λ_{ex} = 510 nm. Inset: fluorescent photoimages in pure DMSO solvent and DMSO/water solution of TCM-DN under light illumination. (c) UV−vis absorption spectra of ABDA in the presence of TCM-DN under light irradiation (0.10 W cm^{-2}, 4 min, 400−700 nm). (d) Normalized absorbance intensity of ABDA at 380 nm after photodecomposition by ROS upon light irradiation.

promising avenue toward reporting specific targeting imaging and an effective therapeutic process for universal poorly permeable tumors.

RESULTS AND DISCUSSION

Constructing Sequence-Activated Nanotheranostics

As mentioned above, PDAC is the most stroma-rich tumor in all solid tumors, and its dense desmoplastic stroma makes it difficult to achieve a better performance by passive targeting or active targeting.[33−35] That is, the current "single-locked" nanotheranostics are unable to alter their targeting properties in the specific intratumoral region, which inevitably limits their tumor distribution. In this case, it is urgent to develop a sequence-activated targeting strategy to break the barrier characterized by low vascularity and dense fibrosis for improving the tumor targeting efficiency of PDAC.

Toward this programmable *in vivo* targeting strategy, peptide-based ligands could be primarily considered as an active targeting unit. Herein, to enhance the specific uptake efficiency of PDAC cells, U11 peptide was chosen due to its high affinity to the PDAC-cell receptors (uPAR).[36−38] In this case, we covalently attached U11 peptides to NIR AIEgen (TCM-DN, emission at 650 nm) to form small AIE nanoparticles with surface-grafted U11 peptides (TCM-U11; Figure 1).[39−43] Subsequently, we chose a diblock copolymer (named $Poly_{pH}$) as a pH-activated nanocarrier, which is composed of a PEG unit and copolymerized hexamethyleneimino-functionalized methacrylate.[44−47] Importantly, this block copolymer $Poly_{pH}$ not only maintains the TCM-U11 inside the nanoparticles in normal tissues but also promises the efficient release of TCM-U11 at the acidic tumor site.

Aiming toward real-time tracking the delivery, distribution, and release of TCM-U11 to PDAC cells without a blind spot, we described a dual-channel NIR fluorescence strategy, that is, TCM-U11 and another NIR indicator Cy (emission at 830 nm) which were coloaded into the $Poly_{pH}$ matrix. Specifically, the dissolved mixture of TCM-U11, Cy, and $Poly_{pH}$ into DMSO was added dropwise into the ultrapure water. Then, the DMSO and unloaded agents were removed via dialysis to obtain uniform TCM-U11&Cy@P nanoparticles. All of the detailed synthetic routes and characterization of TCM-U11, Cy, and $Poly_{pH}$ are depicted in the Supporting Information, and the high-resolution mass spectrometry and ^{1}H NMR measurements were made to fully characterize the peptide-decorated TCM-U11 (Figures S1−S4 in the Supporting Information). Besides, as the controls, we also constructed Cy@P, TCM@P (only TCM-DN loaded), and TCM-U11@P (only TCM-U11 loaded, Figure S5 in the Supporting Information). From the dynamic light scattering (DLS) test, TCM-U11&Cy@P displayed a uniform size of 107 nm (Table S1 in the Supporting Information). Notably, the TCM-U11&Cy@P nanoparticles displayed a uniform size within 72 h, suggesting their excellent stability (Figure S6 in the Supporting Information). The ζ potential value of TCM-U11&Cy@P was 17.8 mV. Moreover, the CMC value was calculated to be only about 0.84 $mgmL^{-1}$, confirming the compact and stable nanostructure of TCM-U11&Cy@P (Figure S7 in the Supporting Information). All of these results indicated that our elaborately designed TCM-U11&Cy@P possessed well-controlled, uniform, and stable nanostructures.

https://doi.org/10.1021/jacsau.1c00553
JACS Au 2022, 2, 246−257

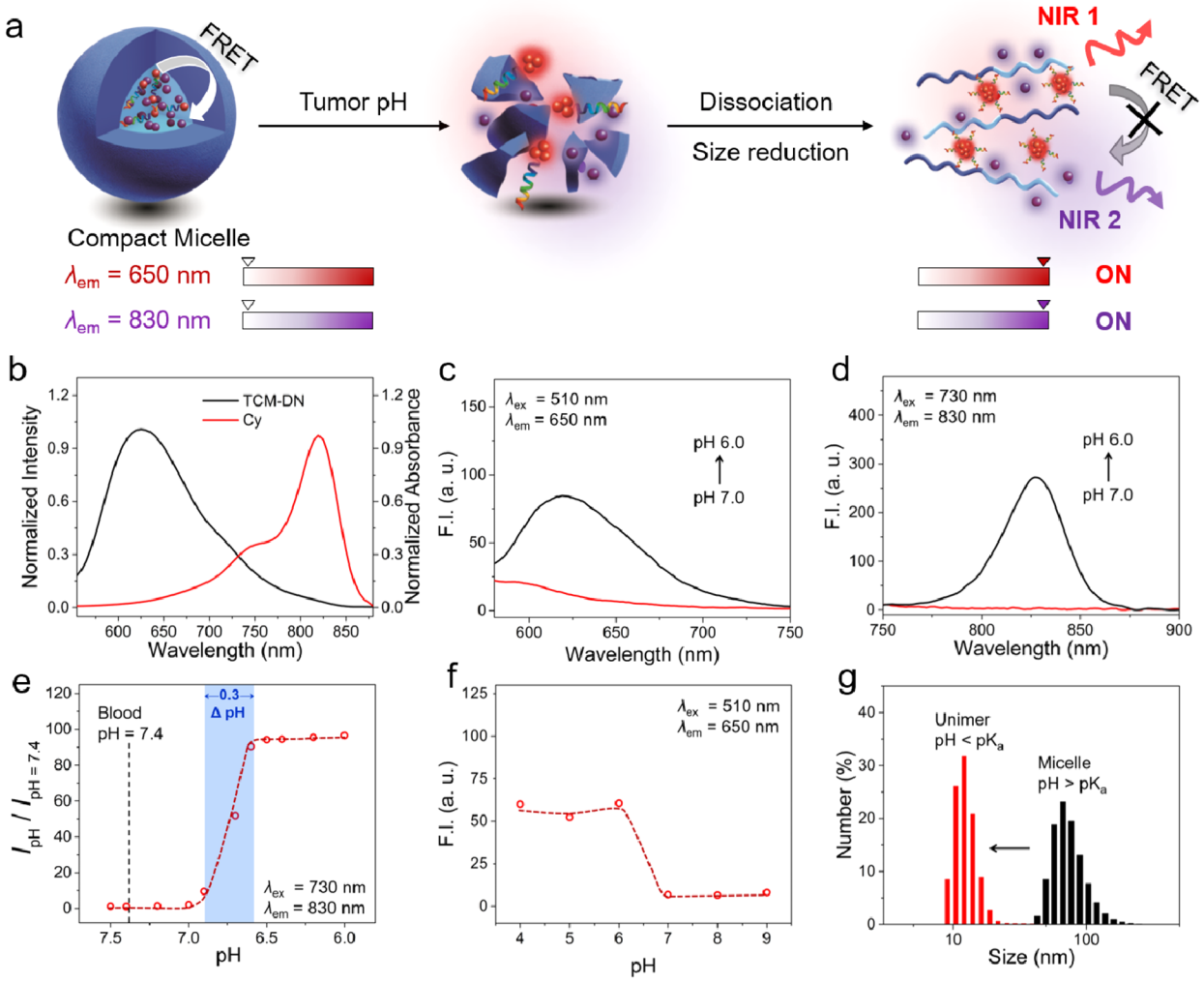

Figure 3. FRET-induced dual-channel response for tracking the sequence-activated process. (a) As is well-known, relatively large nanoparticles (size >50 nm) with the assistance of the EPR effect possess superior tumor accumulation, while relatively small nanoparticles (size <50 nm) could undergo minimal adhesion to the extracellular matrix for improving tumor penetration. Hence, the trade-off effect between tumor accumulation and deep delivery requires a fine regulation of the size and morphology of nanoparticles for sufficient penetration. In our design, the nanotheranostic TCM-U11&Cy@P can disassemble in the acidic tumor microenvironment, alone with the dual-channel response and size transformation. (b) Fluorescence spectra (λ_{ex} = 510 nm, 37 °C) of TCM-DN and excitation spectra (λ_{ex} = 730 nm, 37 °C) of Cy in water/DMSO (f_w = 50 vol %). Fluorescence spectra of TCM-U11&Cy@P in aqueous solution at pH 7.0 and 6.0 at λ_{ex} = 510 nm (c) and λ_{ex} = 730 nm (d). Fluorescence intensity as a function of pH for TCM-U11&Cy@P at 830 nm (e) and 650 nm (f). The nanoprobe displays a sharp pH response (pK_a = 6.8, $\Delta pH_{ON/OFF}$ = 0.3). At pH > pK_a (6.8), the nanoprobe self-assembles as a compact micelle, leading to fluorescence quenching at both 650 and 830 nm. At pH < pK_a (6.8), the nanoprobe can be activated (micelle disassembly) and emits bright fluorescent signals at both 650 and 830 nm. (g) Hydrodynamic diameters of TCM-U11&Cy@P at pH 7.4 and 6.5 in aqueous solution.

Revealing Long-Wavelength AIE Characteristics of TCM-DN

High-fidelity imaging and efficient treatment are of great importance for the PDAC theranostic.[48−52] With this in mind, we chose TCM as the building block for endowing AIEgens with bright NIR emission and excellent photosensitive properties.[53] By introducing electron-donating carbazol and a π-bridge (thiophene unit) into the TCM unit, we obtained the long-wavelength AIEgen TCM-DN. Next, the AIE and PDT characteristics of TCM-DN were investigated (Figure 2). Owing to its hydrophobicity, TCM-DN was highly soluble in DMSO but became an aggregated state in water. With the increasing f_w from 0% to 90%, the fluorescence intensity significantly increased, accompanied by an obvious red shift in emission. In particular, TCM-DN showed strong fluorescence in the mixed f_w = 80% DMSO/water solution in contrast with that in pure DMSO solution, which further confirmed its typical AIE property (Figure 2a,b). Furthermore, to evaluate the reactive oxygen species (ROS) generation capability of TCM-DN, 9,10-anthracenediyl-bis(methylene)-dimalonic acid (ABDA) was utilized as the ROS indicator by the oxidation-induced decrease of absorbance.[54−59] Upon light irradiation with TCM-DN aggregates, the absorption peak of ABDA sharply decreased, confirming the highly efficient production of ROS of TCM-DN (Figure 2c,d). In addition, the time-dependent absorbance of TCM-DN upon continuous illumination demonstrated that it had a 92-fold longer half-life time (~1200 s) than ICG (~13 s, FDA-approved NIR contrast agent). Obviously, TCM-DN exhibited a much better photostability than ICG, demonstrating its great benefit for bioimaging (Figure S8 in the Supporting Information). Moreover, TCM-DN nanoaggregates displayed excellent

https://doi.org/10.1021/jacsau.1c00553
JACS Au 2022, 2, 246−257

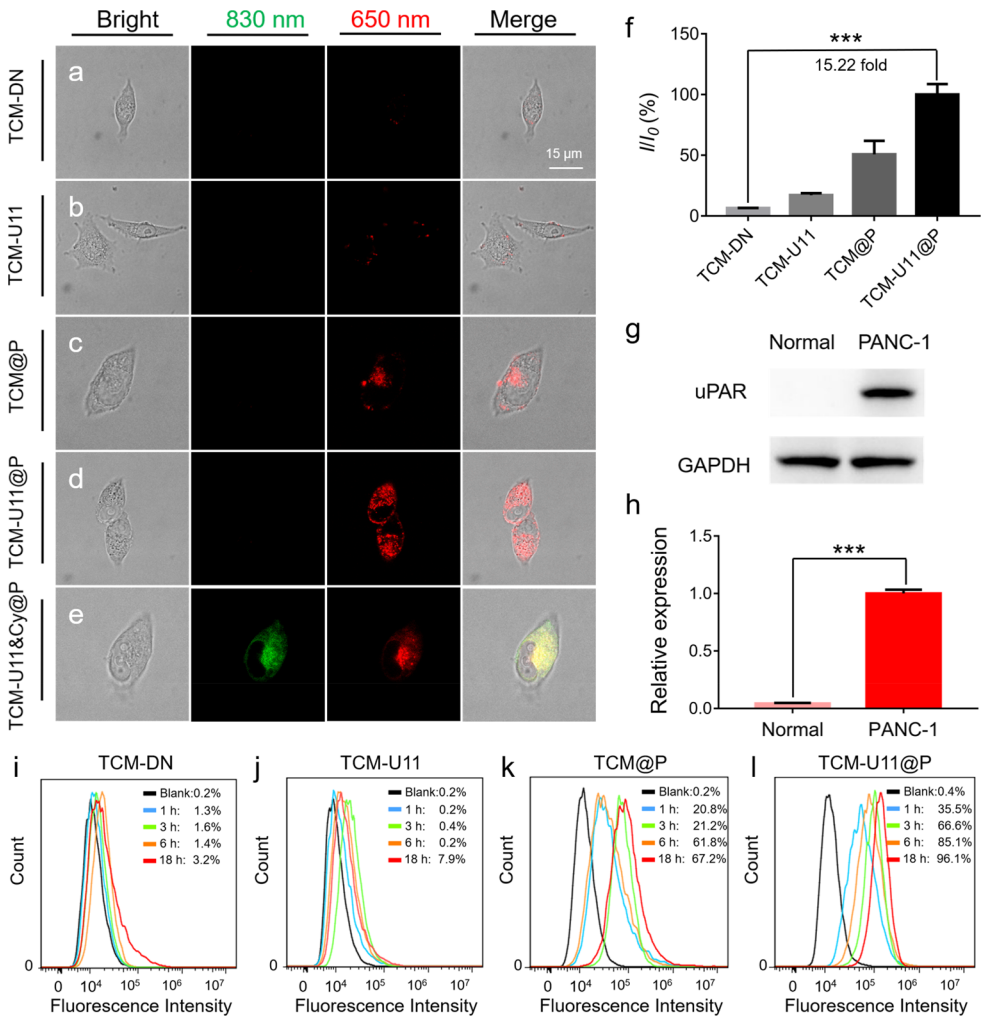

Figure 4. Dual-channel fluorescence for tracking the excellent targeting capability to PANC-1 cells. (a–e) Dual-channel confocal images of PANC-1 cells incubated with TCM-DN, TCM-U11, TCM@P, TCM-U11@P, and TCM-U11&Cy@P. Note: The green channel (λ_{ex} = 730 nm, λ_{em} = 830 nm) indicates the fluorescence from Cy, and the red channel (λ_{ex} = 510 nm, λ_{em} = 650 nm) indicates the fluorescence from TCM-DN. (f) Relative cellular fluorescence intensity under treatment with groups of nanoprobes. Note: Fluorescence images of cells were analyzed by ImageJ software. The experiment is performed three times independently. Data with error bars are expressed as mean ± s.d., n = 3 biologically independent cells. The P value was calculated by the Student's t test. ***$p < 0.001$. (g) Western blot results of uPAR levels between normal MS1 cells and PANC-1 cells. (h) Quantitative analysis of uPAR levels from a Western blot assay. The experiment is performed three times independently, and GAPDH is used as a loading control. ***$p < 0.001$. (i–l) Flow cytometry analysis of cellular uptake of TCM-DN, TCM-U11, TCM@P, and TCM-U11@P in PANC-1 cells.

stability in different pH values (Figure S9 in the Supporting Information). Taken together, our designed TCM-DN showed high-performance AIE and photosensitive properties, indicating its potential capability in high-fidelity bioimaging.

Tracking Sequence-Activated pH-Triggered and Size Transformation Process via Dual-Channel Fluorescence

As is known, most stimuli-responsive nanoparticles suffer from only one "always-ON" readout channel, which makes them unable to understand multistaged behavior in a certain tumor microenvironment in real time.[60−62] In this case, we hypothesized that the Förster resonance energy transfer (FRET) strategy could make a breakthrough for achieving AIE-active responses and thereby implement a real-time monitoring sequence-activated trigger process (Figure 3a and Figure S10 in the Supporting Information).[63−65] In this case, the coloaded longer-wavelength NIR fluorophore Cy (cyanine) was chosen as the quencher (FRET acceptor) of the "always-ON" AIEgen TCM-DN (FRET donor). To confirm the feasibility of this FRET-induced AIE quenching, we then investigated the absorption/fluorescence spectral properties of TCM-DN and Cy units. As expected in Figure 3b and Figure S11 in the Supporting Information, there was a significant spectral overlap between the fluorescence spectrum of TCM-DN and the absorption spectrum of Cy, implying the possibility of a FRET effect from TCM-DN to the Cy moiety.

Encouraged by the aforementioned obvious spectral overlap, we then studied the FRET-induced dual-channel fluorescence responses of TCM-U11&Cy@P with pH change. At pH 7.0, TCM-U11&Cy@P showed nonfluorescence neither at 830 nm (from Cy) nor at 650 nm (from TCM-U11) (Figure 3c,d). This dual emission complete quenching between the two fluorophores could be attributed to the following: (i) TCM-U11&Cy@P formed a compact self-assembled micelle at pH 7.4, leading to the typical aggregation-caused quenching (ACQ) property of Cy in its compact state. (ii) Owing to the FRET effect between TCM-DN and the Cy unit, the

https://doi.org/10.1021/jacsau.1c00553
JACS Au 2022, 2, 246−257

fluorescence of TCM-DN was also effectively quenched from an intermolecular energy transfer.[66,67] Thus, we successfully obtained the AIE fluorescence quenching signal based on the FRET strategy. Given that a pH-response nanocarrier was employed in this nanotheranostic, we reasoned that the change in pH could remarkably influence the efficiency of the FRET process and result in dual-channel fluorescence.

To verify the possibility of the pH-triggered dual-channel fluorescence changes, we further investigated the spectral properties of TCM-U11&Cy@P under acidic conditions. When the pH was decreased to 6.0, the protonation of the hydrophobic block caused the disassembly of the initial compact micelle, leading to a dramatic NIR fluorescence signal enhancement at both 830 and 650 nm (Figure 3c,d). Specifically, the fluorescence intensities at 830 nm (from Cy) and 650 nm (from TCM-U11) were amplified over 80-fold and 8-fold, respectively. Also, the TCM-U11&Cy@P nanoparticles showed an extremely sharp pH response ($\Delta pH_{ON/OFF}$ = 0.3) at pH 6.8 (Figure 3e,f). This significant fluorescence enhancement could be attributed to the following: (i) TCM-U11&Cy@P dissociated in the acidic condition with the release of cyanine dyes, leading to the fluorescence recovery at 830 nm. (ii) TCM-U11 was also released and formed small AIE nanoparticles.[68,69] Consequently, the donor−acceptor distance was beyond the operating range of FRET, resulting in the enhancement of TCM-U11 at 650 nm. All of these results strongly supported the fact that the proposed sequence-activated nanotheranostic TCM-U11&Cy@P had the desired capacity for real-time tracking of the programmed acidic pH-triggered and subsequent size transformation process via dual-channel fluorescence.

To validate the concomitant size responses with the turn-on NIR emission signals at both 830 and 650 nm, we further studied the acidic pH-triggered size response of TCM-U11&Cy@P by transmission electron microscopy (TEM) and dynamic light scattering (DLS). As shown in Figure 3g and Figure S12 in the Supporting Information, with the decreasing of pH value, TCM-U11&Cy@P displayed an obvious size change from 68 to 12 nm, indicating the dissociation of the initial nanoparticles. Also, this acidic-triggered size reduction was consistent with the dual-channel fluorescence responses (Figure 3c−f). Consequently, the size transformable functionality was expected to break the trade-off effect between tumor accumulation and deep delivery required in pancreatic cancer theranostics. Most importantly, the FRET-induced dual-channel fluorescence changes successfully finely regulated the AIE-active signal and thereby made it possible to track the sequence-activated process with high fidelity.

Targeting Pancreatic Cancer Cell with High-Fidelity Imaging

As is well-known, compared with small molecules, nanoparticles could improve intracellular retention and achieve long-time tracking of living cells.[70−74] We thus hypothesized that our designed TCM-U11&Cy@P that combines a well-defined nanostructure and programmable targeting could further promote cellular internalization and imaging performance toward pancreatic cancer cells (PANC-1 cells). In order to evaluate the PANC-1 cell-specific imaging of TCM-U11&Cy@P, we also utilized TCM-DN, TCM-U11, TCM@P (only TCM-DN loaded), and TCM-U11@P (only TCM-U11 loaded) as the controls (Figure S5 in the Supporting Information).

As shown in Figure 4a,b, compared with TCM-DN, TCM-U11 displayed a brighter fluorescence signal in PANC-1 cells, which strongly confirmed the active targeting ability of the U11 peptide. Furthermore, it was found that TCM@P showed a much brighter fluorescence signal than TCM-DN, indicating that the well-defined nanostructure could improve the cell uptake efficiency (Figure 4c and Figure S13 in the Supporting Information). Importantly, TCM-U11@P displayed the brightest AIE fluorescence signal among TCM-DN, TCM-U11, and TCM@P. It was implied that the well-defined nanostructure with a U11 peptide-mediated active targeting ability could execute highly specific PANC-1 cell binding (Figure 4d,f). In TCM-U11&Cy@P, bright NIR signals at both 830 and 650 nm were observed in Figure 4e and Figure S13 in the Supporting Information. In conjunction with the dual-channel imaging results, it could be concluded that we successfully developed a sequence-activated logic nanoprobe for the selective sensing and targeting of PANC-1 cells.

To verify the U11 peptide targeting to the receptors (uPAR) overexpressed on PANC-1 cells, the uPAR levels between normal cells (MS1 cells) and PANC-1 cells were determined by Western blot assays.[75,76] As expected, these results showed the overexpression of uPAR in PANC-1 cells, which was much higher than that of normal cells (Figure 4g,h). Thus, the active targeting of the U11 peptide toward uPAR was effective, confirming the active targeting ability of TCM-U11&Cy@P. All f the cell imaging and Western blot assays demonstrated that the programmable targeting strategy significantly improved the specific targeting ability toward PANC-1 cells.

To quantitatively evaluate the internalization of TCM-U11&Cy@P by PANC-1 cells, the properties of nanoparticles were further analyzed by flow cytometry.[77] First, we evaluated the effect of incubation time on the uptake of PANC-1 cells. As illustrated in Figure 4i, it took 18 h for the cellular uptake ratios of TCM-DN to increase from 0.2% to only 3.2%. Subsequently, we observed the slower uptake ratios of TCM-U11 (7.9%, Figure 4j). In contrast, within only 3 h, the uptake ratios of TCM@P and TCM-U11@P increased to 21.2% and 66.6%, respectively (Figure 4k,l). In particular, TCM-U11@P showed the most significant cell uptake efficiency with the extension of incubation time to 18 h (96.1%). The above flow cytometry analysis results were completely consistent with the *in vitro* confocal imaging results (Figure 4a−f). In addition, we also verified the *in vitro* PDT performance of TCM-U11&Cy@P in cell experiments (Figure S14 in the Supporting Information). Combining all of the above *in vitro* experimental results, the sequence-activated strategy with the incorporation of U11 peptide in TCM-U11@P markedly facilitated cellular internalization of PANC-1 cells and thereby enabled fluorescence imaging with high fidelity.

Revealing Excellent Permeability in a Multicellular 3D Tumor Spheroid

As mentioned above, our designed sequence-activated nanotheranostics TCM-U11&Cy@P could synergistically enhance the targeting ability and permeability to PANC-1 cells. With this in mind, we chose three-dimensional (3D)-structured PANC-1 multicellular tumor spheroids (MCTSs, size: ca. 1 mm) to simulate a PDAC tumor.[78,79] Then, we further evaluated the improved tumor targeting and permeability of TCM-U11&Cy@P in MCTSs. By scanning along the *z*-axis with dual-channel emission at 650 and 830 nm, we recorded fluorescence images in each 9 μm layer of PANC-1 MCTSs

https://doi.org/10.1021/jacsau.1c00553
JACS Au 2022, 2, 246−257

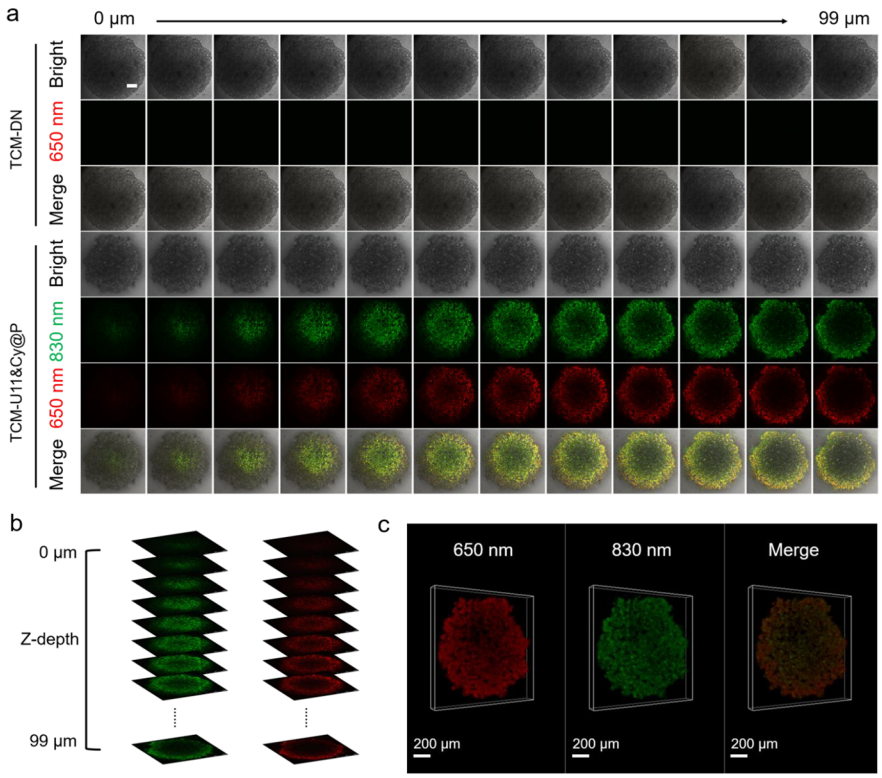

Figure 5. Revealing the permeability: dual-channel *in vitro* imaging of PANC-1 multicellular tumor spheroids. (a, b) Three-dimensional tumor spheroid images obtained along the *z*-axis direction at different depths of PANC-1 MCTSs. Scale bar = 200 μm. Note: green signal, λ_{ex} = 730 nm, λ_{em} = 830 nm; red signal, λ_{ex} = 510 nm, λ_{em} = 650 nm. (c) Three-dimensional reconstruction of confocal microscopy images of PANC-1 MCTSs. Scale bar = 200 μm.

treated with TCM-DN and TCM-U11&Cy@P. As shown in Figure 5a,b, TCM-DN showed a very weak fluorescence signal. In contrast, TCM-U11&Cy@P expressed a visibly brighter and uniformly distributed fluorescence signal in MCTSs, implying much better targeting delivery and efficient penetration. Also, these results further quantitatively confirmed the much better permeability of TCM-U11&Cy@P as compared to TCM-DN (Figure S15 in the Supporting Information). Then, we reconstructed 3D spheroid images through the fluorescence signal of the focal planes. As observed in Figure 5c and Video S1, significant dual-channel fluorescent signals were expressed in the reconstructed 360° rotation video of the 3D-structured spheroids at both 650 and 830 nm. In addition, the *in vivo* FRET process was consistent with *in vitro* experimental results (Figure S16 in the Supporting Information). It is believed that the two channels (830 and 650 nm) are complementary to the imaging output *in vivo* and *in vitro*, greatly improving particular advantages in the bioimaging applications (Figure S17 in the Supporting Information). Clearly, these results highlighted the excellent PDAC tumor targeting and permeability of our sequence-activated nanotheranostic TCM-U11&Cy@P.

Intraoperatively Mapping Human Clinical Specimens with High Resolution

Learning from all of the *in vitro* and *in vivo* results, TCM-U11&Cy@P showed excellent tumor permeability via programmable passive targeting, pH-induced active targeting, and U11 peptide-mediated active targeting. All of these results inspired us to further utilize TCM-U11&Cy@P for mapping human clinical specimens. Therefore, we intraoperatively collected human clinical tissue specimens containing PDAC tissues from patients (pathologically confirmed as PDAC). Patients' pathological Nos. 21579 and 10583 are paraffin sections, and Nos. 00857 and 00841 are frozen sections. These sections were incubated with TCM-U11&Cy@P (16 μM), and then, NIR fluorescence imaging was performed. With the help of high-resolution fluorescence images, the normal tissue and tumor tissue could be rapidly distinguished. In normal tissue, pancreatic lobules with densely arranged normal pancreatic cells were clearly observed (Figure 6a). In contrast, tumor tissue showed malignant histological features including pancreatic cancer embolus and irregular ductlike and tubular structures with glandularly arranged cancer cells. Learning from the fluorescence imaging, the tumor tissue showed significant histological and cell morphological abnormalities compared to the normal tissue (Figure 6c). Synchronously, the H&E staining, a standard histopathological examination, was further conducted. All of the results strongly verified the pathological characteristics in NIR fluorescence imaging (Figure 6b,d). Compared to commercial dye (ICG), TCM-U11&Cy@P exhibited a much higher resolution and significant signal-to-noise (S/N) ratio, further verifying that TCM-U11&Cy@P could map and amplify high-fidelity information in human pancreatic slices (Figure S18 in the Supporting Information). This high-precision and high-fidelity imaging of TCM-U11&Cy@P provided a simple, sensitive, and rapid way to observe the structural differences between the normal tissue and pancreatic cancer tissue.

This high-fidelity imaging also made it an ideal contrast agent for three-dimensional (3D) fluorescence imaging. After incubation with TCM-U11&Cy@P, high-resolution 3D fluorescence images were obtained with a Leica TCS SP8 instrument. As shown in Figure 6e,f, and Video S2, TCM-

https://doi.org/10.1021/jacsau.1c00553
JACS Au 2022, 2, 246−257

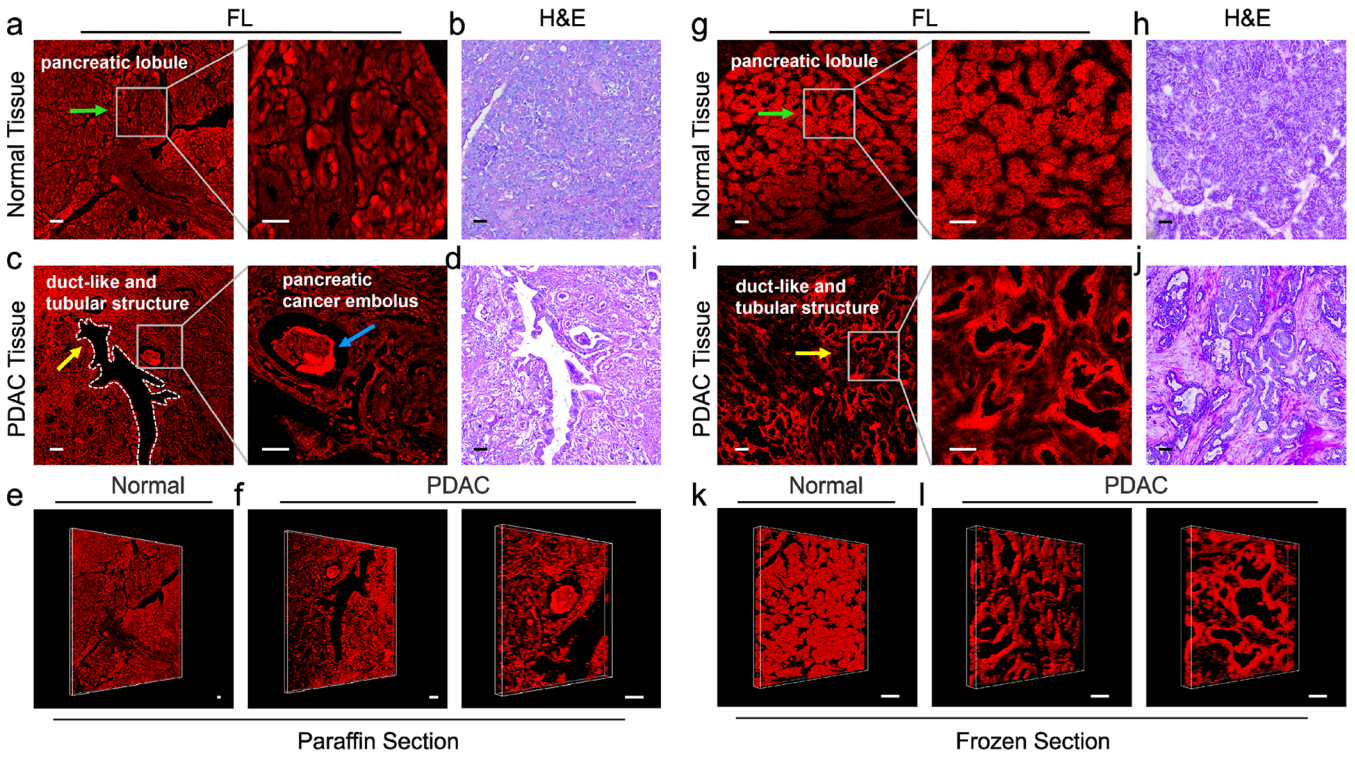

Figure 6. High-resolution three-dimensional fluorescence imaging of human pancreatic sections. We intraoperatively collect clinical tissue specimens containing PDAC tissues from patients (pathologically confirmed as PDAC). Fluorescence imaging (λ_{ex} = 510 nm, λ_{em} = 650 nm) and H&E staining of paraffin sections (a–d) and frozen sections (g–j) with TCM-U11&Cy@P (16 μM). Green arrows indicate a normal pancreatic lobule (with densely arranged pancreatic cells). Yellow arrows indicate malignant elements (irregular ductlike and tubular structures). The blue arrow indicates a pancreatic cancer embolus. PDAC tissue images indicate neoplastic glandular ducts with glandularly arranged cancer cells, showing significant abnormalities in tissue structure and cell morphology. Scale bar = 50 μm. Three-dimensional reconstruction of confocal microscopy images of paraffin sections (e, f) and frozen sections (k, l) along the *z*-axis direction at the depth of 48 μm. Scale bar = 50 μm. Note: Patient's pathological Nos. 21579 and 10583 for panels a–d, Nos. 00857 and 00841 for panels g–j.

U11&Cy@P exhibited strong NIR fluorescence signals in the clinical tissue specimens, thus achieving high-fidelity mapping from different perspectives. Importantly, this 3D fluorescence imaging could also provide more details of longitudinal information. In order to further verify the imaging effect and clinical application value, we also conducted the above imaging experiments on frozen sections. As expected, similar imaging results were also observed with frozen sections (Figure 6g–l and Video S3). All of these results demonstrated that TCM-U11&Cy@P made a breakthrough for rapidly distinguishing human normal tissue and pancreatic cancer tissue via high-fidelity fluorescence imaging.

CONCLUSIONS

In summary, we focused on engineering a programmable targeting strategy of fluorescent nanotheranostics for real-time tracking the delivery across PDAC-specific physical barriers and efficient uptake of deep tumor cells. For the first time, we developed sequence-activated fluorescent nanotheranostic TCM-U1&Cy@P for human pancreatic cancer with an enhanced multitargeting capability: (i) programmable passive targeting, (ii) tumor pH-induced active targeting, and (iii) U11 peptide-mediated active targeting. Ultimately, the released TCM-U11 particles overcome the limitation of dense stroma, allowing for the direct interaction with PDAC cells in the deep tissue for activatable PDT to ablate tumors. The multicellular tumor spheroids and *in vivo* assessments clearly demonstrated that TCM-U11&Cy@P was equipped with potent PDAC-tumor targeting, deep delivery, and phototoxicity. Impressively, FRET-based dual-channel activatable fluorescence was employed for monitoring the programmable targeting process. Most importantly, accompanied by bright NIR emission from the released AIE nanoaggregates inside tumor cells, TCM-U11&Cy@P successfully mapped human clinical specimens with high resolution. The programmable tumor targeting ability of TCM-U11&Cy@P made the breakthrough of tracking across PDAC-specific physical barriers in real time and thereby displayed enhanced tumor permeability. Our study presents a new visualization strategy for the *in vivo* application of intelligent nanotheranostics, paving a new pathway for pancreatic carcinoma.

ASSOCIATED CONTENT

Supporting Information

The Supporting Information is available free of charge at https://pubs.acs.org/doi/10.1021/jacsau.1c00553.

Additional experimental details including the materials, methods, synthetic procedures, characterization data (NMR, HRMS, HPLC, etc.), CMC, ζ potential, photostability, TEM and hydrodynamic diameter of TCM-U11&Cy@P, biofluorescence imaging, high-resolution analysis, and additional data and figures (PDF)

Video S1: Rotation video of a 3D reconstruction of confocal microscopy images of MCTSs (MP4)

Video S2: Rotation video of a 3D reconstruction of confocal microscopy images of paraffin sections (MP4)

https://doi.org/10.1021/jacsau.1c00553
JACS Au 2022, 2, 246–257

Video S3: Rotation video of a 3D reconstruction of confocal microscopy images of frozen sections (MP4)

AUTHOR INFORMATION

Corresponding Authors

Hui Li − *Department of Interventional Radiology, Shanghai Jiao Tong University Affiliated Sixth People's Hospital, Shanghai 200233, China*; Email: huili_doc@163.com

Zhiqian Guo − *Key Laboratory for Advanced Materials and Joint International Research Laboratory of Precision Chemistry and Molecular Engineering, Frontiers Science Center for Materiobiology and Dynamic Chemistry, Shanghai Frontiers Science Center of Optogenetic Techniques for Cell Metabolism, Institute of Fine Chemicals, School of Chemistry and Molecular Engineering, East China University of Science and Technology, Shanghai 200237, China*; orcid.org/0000-0002-2192-825X; Email: guozq@ecust.edu.cn

Authors

Yining Tao − *Department of Interventional Radiology, Shanghai Jiao Tong University Affiliated Sixth People's Hospital, Shanghai 200233, China; Key Laboratory for Advanced Materials and Joint International Research Laboratory of Precision Chemistry and Molecular Engineering, Frontiers Science Center for Materiobiology and Dynamic Chemistry, Shanghai Frontiers Science Center of Optogenetic Techniques for Cell Metabolism, Institute of Fine Chemicals, School of Chemistry and Molecular Engineering, East China University of Science and Technology, Shanghai 200237, China*

Chenxu Yan − *Key Laboratory for Advanced Materials and Joint International Research Laboratory of Precision Chemistry and Molecular Engineering, Frontiers Science Center for Materiobiology and Dynamic Chemistry, Shanghai Frontiers Science Center of Optogenetic Techniques for Cell Metabolism, Institute of Fine Chemicals, School of Chemistry and Molecular Engineering, East China University of Science and Technology, Shanghai 200237, China*

Dan Li − *Key Laboratory for Advanced Materials and Joint International Research Laboratory of Precision Chemistry and Molecular Engineering, Frontiers Science Center for Materiobiology and Dynamic Chemistry, Shanghai Frontiers Science Center of Optogenetic Techniques for Cell Metabolism, Institute of Fine Chemicals, School of Chemistry and Molecular Engineering, East China University of Science and Technology, Shanghai 200237, China*

Jianfeng Dai − *Key Laboratory for Advanced Materials and Joint International Research Laboratory of Precision Chemistry and Molecular Engineering, Frontiers Science Center for Materiobiology and Dynamic Chemistry, Shanghai Frontiers Science Center of Optogenetic Techniques for Cell Metabolism, Institute of Fine Chemicals, School of Chemistry and Molecular Engineering, East China University of Science and Technology, Shanghai 200237, China*

Yingsheng Cheng − *Department of Interventional Radiology, Shanghai Jiao Tong University Affiliated Sixth People's Hospital, Shanghai 200233, China*

Wei-Hong Zhu − *Key Laboratory for Advanced Materials and Joint International Research Laboratory of Precision Chemistry and Molecular Engineering, Frontiers Science Center for Materiobiology and Dynamic Chemistry, Shanghai Frontiers Science Center of Optogenetic Techniques for Cell Metabolism, Institute of Fine Chemicals, School of Chemistry and Molecular Engineering, East China University of Science and Technology, Shanghai 200237, China*; orcid.org/0000-0001-9103-166X

Complete contact information is available at: https://pubs.acs.org/10.1021/jacsau.1c00553

Author Contributions

‖Y.T. and C.Y. contributed equally to this work.

Notes

The authors declare no competing financial interest.

ACKNOWLEDGMENTS

This work was supported by National Key Research and Development Program of China (2021YFA0910000), NSFC/China (21788102, 81571773, 81771943, 81971714, 21878087, and 21908060), Shanghai Municipal Science and Technology Major Project (Grant 2018SHZDZX03), Shanghai Municipal Education Commission (2021 Sci&Tech 03-28), and the Shuguang Program (18SG27). The patients were pathologically confirmed as pancreatic ductal adenocarcinoma at the Shanghai Jiao Tong University Affiliated Sixth People's Hospital. The written informed consent was obtained, and the protocol was approved by the Review Board of the Shanghai Jiao Tong University Affiliated Sixth People's Hospital (Approval 2021-087). The pathological specimens were immediately frozen or embedded in paraffin after being obtained.

REFERENCES

(1) De Lazaro, I.; Mooney, D. J. Obstacles and opportunities in a forward vision for cancer nanomedicine. *Nat. Mater.* **2021**, *20*, 1469−1479.

(2) Cabral, H.; Matsumoto, Y.; Mizuno, K.; Chen, Q.; Murakami, M.; Kimura, M.; Terada, Y.; Kano, M. R.; Miyazono, K.; Uesaka, M.; Nishiyama, N.; Kataoka, K. Accumulation of sub-100 nm polymeric micelles in poorly permeable tumours depends on size. *Nat. Nanotechnol.* **2011**, *6*, 815−23.

(3) Wang, G.; Zhou, Z.; Zhao, Z.; Li, Q.; Wu, Y.; Yan, S.; Shen, Y.; Huang, P. Enzyme-triggered transcytosis of dendrimer-drug conjugate for deep penetration into pancreatic tumors. *ACS Nano* **2020**, *14*, 4890−4904.

(4) Giordano, G.; Pancione, M.; Olivieri, N.; Parcesepe, P.; Velocci, M.; Raimo, T. D.; Coppola, L.; Toffoli, G.; D'Andrea, M. R. Nano albumin bound-paclitaxel in pancreatic cancer: Current evidences and future directions. *World J. Gastroenterol.* **2017**, *23*, 5875−5886.

(5) Siegel, R. L.; Miller, K. D.; Fuchs, H. E.; Jemal, A. Cancer statistics, 2021. *CA Cancer J. Clin.* **2021**, *71*, 7−33.

(6) Kleeff, J.; Korc, M.; Apte, M.; La Vecchia, C.; Johnson, C. D.; Biankin, A. V.; Neale, R. E.; Tempero, M.; Tuveson, D. A.; Hruban, R. H.; Neoptolemos, J. P. Pancreatic cancer. *Nat. Rev. Dis. Primers* **2016**, *2*, 16022.

(7) Alonso-Curbelo, D.; Ho, Y. J.; Burdziak, C.; Maag, J. L. V.; Morris, J. P. t.; Chandwani, R.; Chen, H. A.; Tsanov, K. M.; Barriga, F. M.; Luan, W.; Tasdemir, N.; Livshits, G.; Azizi, E.; Chun, J.; Wilkinson, J. E.; Mazutis, L.; Leach, S. D.; Koche, R.; Pe'er, D.; Lowe, S. W. A gene-environment-induced epigenetic program initiates tumorigenesis. *Nature* **2021**, *590*, 642−648.

(8) Tempero, M. A.; Berlin, J.; Ducreux, M.; Haller, D.; Harper, P.; Khayat, D.; Schmoll, H. J.; Sobrero, A.; Van Cutsem, E. Pancreatic cancer treatment and research: an international expert panel discussion. *Ann. Oncol.* **2011**, *22*, 1500−1506.

(9) Wu, Y.; Huang, S.; Wang, J.; Sun, L.; Zeng, F.; Wu, S. Activatable probes for diagnosing and positioning liver injury and metastatic

tumors by multispectral optoacoustic tomography. *Nat. Commun.* **2018**, *9*, 3983.
(10) Meng, Z.; Zhou, X.; Xu, J.; Han, X.; Dong, Z.; Wang, H.; Zhang, Y.; She, J.; Xu, L.; Wang, C.; Liu, Z. Light-triggered in situ gelation to enable robust photodynamic-immunotherapy by repeated stimulations. *Adv. Mater.* **2019**, *31*, 1900927.
(11) Gao, J.; Li, J.; Geng, W. C.; Chen, F. Y.; Duan, X.; Zheng, Z.; Ding, D.; Guo, D. S. Biomarker displacement activation: a general host-guest strategy for targeted phototheranostics *in vivo*. *J. Am. Chem. Soc.* **2018**, *140*, 4945−4953.
(12) Chen, X.; Gao, H.; Deng, Y.; Jin, Q.; Ji, J.; Ding, D. Supramolecular aggregation-induced emission nanodots with programmed tumor microenvironment responsiveness for image-guided orthotopic pancreatic cancer therapy. *ACS Nano* **2020**, *14*, 5121−5134.
(13) Han, H.; Hou, Y.; Chen, X.; Zhang, P.; Kang, M.; Jin, Q.; Ji, J.; Gao, M. Metformin-induced stromal depletion to enhance the penetration of Gemcitabine-loaded magnetic nanoparticles for pancreatic cancer targeted therapy. *J. Am. Chem. Soc.* **2020**, *142*, 4944−4954.
(14) Shi, Y.; Gao, W.; Lytle, N. K.; Huang, P.; Yuan, X.; Dann, A. M.; Ridinger-Saison, M.; DelGiorno, K. E.; Antal, C. E.; Liang, G.; Atkins, A. R.; Erikson, G.; Sun, H.; Meisenhelder, J.; Terenziani, E.; Woo, G.; Fang, L.; Santisakultarm, T. P.; Manor, U.; Xu, R.; Becerra, C. R.; Borazanci, E.; Von Hoff, D. D.; Grandgenett, P. M.; Hollingsworth, M. A.; Leblanc, M.; Umetsu, S. E.; Collisson, E. A.; Scadeng, M.; Lowy, A. M.; Donahue, T. R.; Reya, T.; Downes, M.; Evans, R. M.; Wahl, G. M.; Pawson, T.; Tian, R.; Hunter, T. Targeting LIF-mediated paracrine interaction for pancreatic cancer therapy and monitoring. *Nature* **2019**, *569*, 131−135.
(15) Wu, X.; Liu, H.; Han, D.; Peng, B.; Zhang, H.; Zhang, L.; Li, J.; Liu, J.; Cui, C.; Fang, S.; Li, M.; Ye, M.; Tan, W. Elucidation and structural modeling of CD71 as a molecular target for cell-specific aptamer binding. *J. Am. Chem. Soc.* **2019**, *141*, 10760−10769.
(16) Zheng, R.; Yang, J.; Mamuti, M.; Hou, D. Y.; An, H. W.; Zhao, Y.; Wang, H. Controllable self-assembly of peptide-cyanine conjugates *in vivo* as fine-tunable theranostics. *Angew. Chem., Int. Ed.* **2021**, *60*, 7809−7819.
(17) Yan, Y.; Chen, B.; Wang, Z.; Yin, Q.; Wang, Y.; Wan, F.; Mo, Y.; Xu, B.; Zhang, Q.; Wang, S.; Wang, Y. Sequential modulations of tumor vasculature and stromal barriers augment the active targeting efficacy of antibody-modified nanophotosensitizer in desmoplastic ovarian carcinoma. *Adv. Sci.* **2021**, *8*, 2002253.
(18) Yang, G.; Phua, S. Z. F.; Lim, W. Q.; Zhang, R.; Feng, L.; Liu, G.; Wu, H.; Bindra, A. K.; Jana, D.; Liu, Z.; Zhao, Y. A hypoxia-responsive albumin-based nanosystem for deep tumor penetration and excellent therapeutic efficacy. *Adv. Mater.* **2019**, *31*, 1901513.
(19) He, S.; Li, J.; Lyu, Y.; Huang, J.; Pu, K. Near-infrared fluorescent macromolecular reporters for real-time imaging and urinalysis of cancer immunotherapy. *J. Am. Chem. Soc.* **2020**, *142*, 7075−7082.
(20) Li, X.; Park, E. Y.; Kang, Y.; Kwon, N.; Yang, M.; Lee, S.; Kim, W. J.; Kim, C.; Yoon, J. Supramolecular phthalocyanine assemblies for improved photoacoustic imaging and photothermal therapy. *Angew. Chem., Int. Ed.* **2020**, *59*, 8630−8634.
(21) Wang, Y.; Shi, L.; Wu, W.; Qi, G.; Zhu, X.; Liu, B. Tumor-activated photosensitization and size transformation of nanodrugs. *Adv. Funct. Mater.* **2021**, *31*, 2010241.
(22) Wang, Y.; Zhou, K.; Huang, G.; Hensley, C.; Huang, X.; Ma, X.; Zhao, T.; Sumer, B. D.; DeBerardinis, R. J.; Gao, J. A nanoparticle-based strategy for the imaging of a broad range of tumours by nonlinear amplification of microenvironment signals. *Nat. Mater.* **2014**, *13*, 204−12.
(23) An, H. W.; Li, L. L.; Wang, Y.; Wang, Z.; Hou, D.; Lin, Y. X.; Qiao, S. L.; Wang, M. D.; Yang, C.; Cong, Y.; Ma, Y.; Zhao, X. X.; Cai, Q.; Chen, W. T.; Lu, C. Q.; Xu, W.; Wang, H.; Zhao, Y. A tumour-selective cascade activatable self-detained system for drug delivery and cancer imaging. *Nat. Commun.* **2019**, *10*, 4861.
(24) Zhang, Y.; Yan, C.; Wang, C.; Guo, Z.; Liu, X.; Zhu, W. H. A sequential dual-lock strategy for photoactivatable chemiluminescent probes enabling bright duplex optical imaging. *Angew. Chem., Int. Ed.* **2020**, *59*, 9059−9066.
(25) Yan, C.; Guo, Z.; Liu, Y.; Shi, P.; Tian, H.; Zhu, W. H. A sequence-activated AND logic dual-channel fluorescent probe for tracking programmable drug release. *Chem. Sci.* **2018**, *9*, 6176−6182.
(26) Ren, T. B.; Wang, Z. Y.; Xiang, Z.; Lu, P.; Lai, H. H.; Yuan, L.; Zhang, X. B.; Tan, W. A general strategy for development of activatable NIR-II fluorescent probes for *in vivo* high-contrast bioimaging. *Angew. Chem., Int. Ed.* **2021**, *60*, 800−805.
(27) Zhang, D.; Wang, L.; Yuan, X.; Gong, Y.; Liu, H.; Zhang, J.; Zhang, X.; Liu, Y.; Tan, W. Naked-eye readout of analyte-induced NIR fluorescence responses by an initiation-input-transduction nanoplatform. *Angew. Chem., Int. Ed.* **2020**, *59*, 695−699.
(28) Yan, C.; Shi, L.; Guo, Z.; Zhu, W. Molecularly near-infrared fluorescent theranostics for *in vivo* tracking tumor-specific chemotherapy. *Chin. Chem. Lett.* **2019**, *30*, 1849−1855.
(29) Huang, H.; Yu, C.; Li, X.; Zhang, Y.; Zhang, Y.; Chen, X.; Mariano, P.; Xie, H.; Wang, W. Synthesis of aldehydes by organocatalytic formylation reactions of boronic acids with glyoxylic acid. *Angew. Chem., Int. Ed.* **2017**, *56*, 8201−8205.
(30) Wu, L.; Huang, J.; Pu, K.; James, T. D. Dual-locked spectroscopic probes for sensing and therapy. *Nat. Rev. Chem.* **2021**, *5*, 406−421.
(31) Li, X.; Fan, H.; Guo, T.; Bai, H.; Kwon, N.; Kim, K. H.; Yu, S.; Cho, Y.; Kim, H.; Nam, K. T.; Yoon, J.; Zhang, X. B.; Tan, W. Sequential protein-responsive nanophotosensitizer complex for enhancing tumor-specific therapy. *ACS Nano* **2019**, *13*, 6702−6710.
(32) Ma, Y.; Yan, C.; Guo, Z.; Tan, G.; Niu, D.; Li, Y.; Zhu, W. H. Spatio-temporally reporting dose-dependent chemotherapy via uniting dual-modal MRI/NIR imaging. *Angew. Chem., Int. Ed.* **2020**, *59*, 21143−21150.
(33) Ji, T.; Lang, J.; Wang, J.; Cai, R.; Zhang, Y.; Qi, F.; Zhang, L.; Zhao, X.; Wu, W.; Hao, J.; Qin, Z.; Zhao, Y.; Nie, G. Designing Liposomes To Suppress Extracellular Matrix Expression To Enhance Drug Penetration and Pancreatic Tumor Therapy. *ACS Nano* **2017**, *11*, 8668−8678.
(34) Kota, J.; Hancock, J.; Kwon, J.; Korc, M. Pancreatic cancer: Stroma and its current and emerging targeted therapies. *Cancer Lett.* **2017**, *391*, 38−49.
(35) Sun, Q.; Zhou, Z.; Qiu, N.; Shen, Y. Rational design of cancer nanomedicine: nanoproperty integration and synchronization. *Adv. Mater.* **2017**, *29*, 1606628.
(36) Li, Q.; Li, S.; He, S.; Chen, W.; Cheng, P.; Zhang, Y.; Miao, Q.; Pu, K. An activatable polymeric reporter for near-infrared fluorescent and photoacoustic imaging of invasive cancer. *Angew. Chem., Int. Ed.* **2020**, *59*, 7018−7023.
(37) Hong, Y.; Che, S.; Hui, B.; Yang, Y.; Wang, X.; Zhang, X.; Qiang, Y.; Ma, H. Lung cancer therapy using doxorubicin and curcumin combination: Targeted prodrug based, pH sensitive nanomedicine. *Biomed. Pharmacother.* **2019**, *112*, 108614.
(38) Li, H.; Wang, P.; Gong, W.; Wang, Q.; Zhou, J.; Zhu, W. H.; Cheng, Y. Dendron-Grafted Polylysine-Based Dual-Modal Nanoprobe for Ultra-Early Diagnosis of Pancreatic Precancerosis via Targeting a Urokinase-Type Plasminogen Activator Receptor. *Adv. Healthc. Mater.* **2018**, *7*, 1700912.
(39) Chen, H.; Li, S.; Wu, M.; Kenry Huang, Z.; Lee, C. S.; Liu, B. Membrane-anchoring photosensitizer with aggregation-induced emission characteristics for combating multidrug-resistant bacteria. *Angew. Chem., Int. Ed.* **2020**, *59*, 632−636.
(40) Liu, P.; Fu, W.; Verwilst, P.; Won, M.; Shin, J.; Cai, Z.; Tong, B.; Shi, J.; Dong, Y.; Kim, J. S. MDM2-associated clusterization-triggered emission and apoptosis induction effectuated by a theranostic spiropolymer. *Angew. Chem., Int. Ed.* **2020**, *59*, 8435−8439.
(41) Xu, W.; Lee, M. M. S.; Nie, J. J.; Zhang, Z.; Kwok, R. T. K.; Lam, J. W. Y.; Xu, F. J.; Wang, D.; Tang, B. Z. Three-pronged attack by homologous far-red/NIR AIEgens to achieve 1 + 1+1 > 3

https://doi.org/10.1021/jacsau.1c00553
JACS Au 2022, 2, 246−257

synergistic enhanced photodynamic therapy. *Angew. Chem., Int. Ed.* **2020**, *59*, 9610−9616.
(42) He, X.; Yang, Y.; Guo, Y.; Lu, S.; Du, Y.; Li, J. J.; Zhang, X.; Leung, N. L. C.; Zhao, Z.; Niu, G.; Yang, S.; Weng, Z.; Kwok, R. T. K.; Lam, J. W. Y.; Xie, G.; Tang, B. Z. Phage-guided targeting, discriminative imaging, and synergistic killing of bacteria by AIE bioconjugates. *J. Am. Chem. Soc.* **2020**, *142*, 3959−3969.
(43) Yan, C.; Xu, H.; Wu, M.; Zhao, Z.; Zhao, W.; Tang, J.; Guo, Z. Engineering molecular self-assembly of theranostic nanoprobes for dual-modal imaging-guided precise chemotherapy. *Sci. China Chem.* **2021**, *64*, 2045.
(44) Liu, X.; Liang, X.; Hu, Y.; Han, L.; Qu, Q.; Liu, D.; Guo, J.; Zeng, Z.; Bai, H.; Kwok, R. T. K.; Qin, A.; Lam, J. W. Y.; Tang, B. Z. Catalyst-Free Spontaneous polymerization with 100% atom economy: facile synthesis of photoresponsive polysulfonates with multifunctionalities. *JACS Au* **2021**, *1*, 344−353.
(45) Wang, Z.; Ju, Y.; Ali, Z.; Yin, H.; Sheng, F.; Lin, J.; Wang, B.; Hou, Y. Near-infrared light and tumor microenvironment dual responsive size-switchable nanocapsules for multimodal tumor theranostics. *Nat. Commun.* **2019**, *10*, 4418.
(46) Feng, H. T.; Li, Y.; Duan, X.; Wang, X.; Qi, C.; Lam, J. W. Y.; Ding, D.; Tang, B. Z. Substitution activated precise phototheranostics through supramolecular assembly of AIEgen and calixarene. *J. Am. Chem. Soc.* **2020**, *142*, 15966−15974.
(47) Wang, X.; Wilhelm, J.; Li, W.; Li, S.; Wang, Z.; Huang, G.; Wang, J.; Tang, H.; Khorsandi, S.; Sun, Z.; Evers, B.; Gao, J. Polycarbonate-based ultra-pH sensitive nanoparticles improve therapeutic window. *Nat. Commun.* **2020**, *11*, 5828.
(48) Peng, J.; Samanta, A.; Zeng, X.; Han, S.; Wang, L.; Su, D.; Loong, D. T.; Kang, N. Y.; Park, S. J.; All, A. H.; Jiang, W.; Yuan, L.; Liu, X.; Chang, Y. T. Real-time *in vivo* hepatotoxicity monitoring through chromophore-conjugated photon-upconverting nanoprobes. *Angew. Chem., Int. Ed.* **2017**, *56*, 4165−4169.
(49) Scott, J. I.; Gutkin, S.; Green, O.; Thompson, E. J.; Kitamura, T.; Shabat, D.; Vendrell, M. A functional chemiluminescent probe for *in vivo* imaging of natural killer cell activity against tumours. *Angew. Chem., Int. Ed.* **2021**, *60*, 5699−5703.
(50) Lukinavicius, G.; Reymond, L.; Umezawa, K.; Sallin, O.; D'Este, E.; Gottfert, F.; Ta, H.; Hell, S. W.; Urano, Y.; Johnsson, K. Fluorogenic probes for multicolor imaging in living cells. *J. Am. Chem. Soc.* **2016**, *138*, 9365−8.
(51) Wu, X.; Wang, R.; Qi, S.; Kwon, N.; Han, J.; Kim, H.; Li, H.; Yu, F.; Yoon, J. Rational design of a highly selective near-infrared two-photon fluorogenic probe for imaging orthotopic hepatocellular carcinoma chemotherapy. *Angew. Chem., Int. Ed.* **2021**, *60*, 15418−15425.
(52) Lin, T. C.; Liu, Z. Y.; Liu, S. H.; Koshevoy, I. O.; Chou, P. T. Counterion migration driven by light-induced intramolecular charge transfer. *JACS Au* **2021**, *1*, 282−293.
(53) Zhang, J.; Wang, Q.; Guo, Z.; Zhang, S.; Yan, C.; Tian, H.; Zhu, W. H. High-fidelity trapping of spatial-temporal mitochondria with rational design of aggregation-induced emission probes. *Adv. Funct. Mater.* **2019**, *29*, 1808153.
(54) Murfin, L. C.; Weber, M.; Park, S. J.; Kim, W. T.; Lopez-Alled, C. M.; McMullin, C. L.; Pradaux-Caggiano, F.; Lyall, C. L.; Kociok-Kohn, G.; Wenk, J.; Bull, S. D.; Yoon, J.; Kim, H. M.; James, T. D.; Lewis, S. E. Azulene-derived fluorescent probe for bioimaging: detection of reactive oxygen and nitrogen species by two-photon microscopy. *J. Am. Chem. Soc.* **2019**, *141*, 19389−19396.
(55) Zhao, X.; Long, S.; Li, M.; Cao, J.; Li, Y.; Guo, L.; Sun, W.; Du, J.; Fan, J.; Peng, X. Oxygen-dependent regulation of excited-state deactivation process of rational photosensitizer for smart phototherapy. *J. Am. Chem. Soc.* **2020**, *142*, 1510−1517.
(56) Li, M.; Shao, Y.; Kim, J. H.; Pu, Z.; Zhao, X.; Huang, H.; Xiong, T.; Kang, Y.; Li, G.; Shao, K.; Fan, J.; Foley, J. W.; Kim, J. S.; Peng, X. Unimolecular photodynamic o2-economizer to overcome hypoxia resistance in phototherapeutics. *J. Am. Chem. Soc.* **2020**, *142*, 5380−5388.
(57) Won, M.; Koo, S.; Li, H.; Sessler, J. L.; Lee, J. Y.; Sharma, A.; Kim, J. S. An ethacrynic acid-brominated BODIPY photosensitizer (EA-BPS) construct enhances the lethality of reactive oxygen species in hypoxic tumor-targeted photodynamic therapy. *Angew. Chem., Int. Ed.* **2021**, *60*, 3196−3204.
(58) Qi, J.; Chen, C.; Zhang, X.; Hu, X.; Ji, S.; Kwok, R. T. K.; Lam, J. W. Y.; Ding, D.; Tang, B. Z. Light-driven transformable optical agent with adaptive functions for boosting cancer surgery outcomes. *Nat. Commun.* **2018**, *9*, 1848.
(59) Wang, S.; Tian, R.; Zhang, X.; Cheng, G.; Yu, P.; Chang, J.; Chen, X. Beyond photo: xdynamic therapies in fighting cancer. *Adv. Mater.* **2021**, *33*, 2007488.
(60) Li, H.; Kim, D.; Yao, Q.; Ge, H.; Chung, J.; Fan, J.; Wang, J.; Peng, X.; Yoon, J. Activity-based NIR enzyme fluorescent probes for the diagnosis of tumors and image-guided surgery. *Angew. Chem., Int. Ed.* **2021**, *60*, 17268−17289.
(61) Yin, Q.; Pan, A.; Chen, B.; Wang, Z.; Tang, M.; Yan, Y.; Wang, Y.; Xia, H.; Chen, W.; Du, H.; Chen, M.; Fu, C.; Wang, Y.; Yuan, X.; Lu, Z.; Zhang, Q.; Wang, Y. Quantitative imaging of intracellular nanoparticle exposure enables prediction of nanotherapeutic efficacy. *Nat. Commun.* **2021**, *12*, 2385.
(62) Guo, Z.; Yan, C.; Zhu, W. H. High-performance quinoline-malononitrile core as a building block for the diversity-oriented synthesis of AIEgens. *Angew. Chem., Int. Ed.* **2020**, *59*, 9812−9825.
(63) Li, Q. L.; Wang, D.; Cui, Y.; Fan, Z.; Ren, L.; Li, D.; Yu, J. AIEgen-functionalized mesoporous silica gated by cyclodextrin-modified CuS for cell imaging and chemo-photothermal cancer therapy. *ACS Appl. Mater. Interfaces* **2018**, *10*, 12155−12163.
(64) Xi, D.; Xiao, M.; Cao, J.; Zhao, L.; Xu, N.; Long, S.; Fan, J.; Shao, K.; Sun, W.; Yan, X.; Peng, X. NIR light-driving barrier-free group rotation in nanoparticles with an 88.3% photothermal conversion efficiency for photothermal therapy. *Adv. Mater.* **2020**, *32*, 1907855.
(65) Cheng, D.; Pan, Y.; Wang, L.; Zeng, Z.; Yuan, L.; Zhang, X.; Chang, Y. T. Selective visualization of the endogenous peroxynitrite in an inflamed mouse model by a mitochondria-targetable two-photon ratiometric fluorescent probe. *J. Am. Chem. Soc.* **2017**, *139*, 285−292.
(66) Wang, L.; Tran, M.; D'Este, E.; Roberti, J.; Koch, B.; Xue, L.; Johnsson, K. A general strategy to develop cell permeable and fluorogenic probes for multicolour nanoscopy. *Nat. Chem.* **2020**, *12*, 165−172.
(67) Zhao, M.; Wang, J.; Lei, Z.; Lu, L.; Wang, S.; Zhang, H.; Li, B.; Zhang, F. NIR-II pH sensor with a FRET adjustable transition point for in situ dynamic tumor microenvironment visualization. *Angew. Chem., Int. Ed.* **2021**, *60*, 5091−5095.
(68) Zhao, Z.; Zheng, X.; Du, L.; Xiong, Y.; He, W.; Gao, X.; Li, C.; Liu, Y.; Xu, B.; Zhang, J.; Song, F.; Yu, Y.; Zhao, X.; Cai, Y.; He, X.; Kwok, R. T. K.; Lam, J. W. Y.; Huang, X.; Lee Phillips, D.; Wang, H.; Tang, B. Z. Non-aromatic annulene-based aggregation-induced emission system via aromaticity reversal process. *Nat. Commun.* **2019**, *10*, 2952.
(69) Yan, C.; Guo, Z.; Chi, W.; Fu, W.; Abedi, S. A. A.; Liu, X.; Tian, H.; Zhu, W. H. Fluorescence umpolung enables light-up sensing of N-acetyltransferases and nerve agents. *Nat. Commun.* **2021**, *12*, 3869.
(70) Tian, M.; Sun, J.; Dong, B.; Lin, W. Dynamically monitoring cell viability in a dual-color mode: construction of an aggregation/monomer-based probe capable of reversible mitochondria-nucleus migration. *Angew. Chem., Int. Ed.* **2018**, *57*, 16506−16510.
(71) Xuan, W.; Xia, Y.; Li, T.; Wang, L.; Liu, Y.; Tan, W. Molecular self-assembly of bioorthogonal aptamer-prodrug conjugate micelles for hydrogen peroxide and ph-independent cancer chemodynamic therapy. *J. Am. Chem. Soc.* **2020**, *142*, 937−944.
(72) Zhang, Z.; Qiu, N.; Wu, S.; Liu, X.; Zhou, Z.; Tang, J.; Liu, Y.; Zhou, R.; Shen, Y. Dose-independent transfection of hydrophobized polyplexes. *Adv. Mater.* **2021**, *33*, 2102219.
(73) Zhang, Q.; Mayoral, A.; Terasaki, O.; Zhang, Q.; Ma, B.; Zhao, C.; Yang, G.; Yu, J. Amino acid-assisted construction of single-crystalline hierarchical nanozeolites via oriented-aggregation and intraparticle ripening. *J. Am. Chem. Soc.* **2019**, *141*, 3772−3776.

https://doi.org/10.1021/jacsau.1c00553
JACS Au 2022, 2, 246−257

(74) Yu, J.; Zhao, F.; Gao, W.; Yang, X.; Ju, Y.; Zhao, L.; Guo, W.; Xie, J.; Liang, X. J.; Tao, X.; Li, J.; Ying, Y.; Li, W.; Zheng, J.; Qiao, L.; Xiong, S.; Mou, X.; Che, S.; Hou, Y. Magnetic reactive oxygen species nanoreactor for switchable magnetic resonance imaging guided cancer therapy based on ph-sensitive Fe_5C_2@Fe_3O_4 nanoparticles. *ACS Nano* **2019**, *13*, 10002−10014.
(75) Sharma, A.; Lee, M. G.; Won, M.; Koo, S.; Arambula, J. F.; Sessler, J. L.; Chi, S. G.; Kim, J. S. Targeting heterogeneous tumors using a multifunctional molecular prodrug. *J. Am. Chem. Soc.* **2019**, *141*, 15611−15618.
(76) Ning, J.; Liu, T.; Dong, P.; Wang, W.; Ge, G.; Wang, B.; Yu, Z.; Shi, L.; Tian, X.; Huo, X.; Feng, L.; Wang, C.; Sun, C.; Cui, J.; James, T. D.; Ma, X. Molecular design strategy to construct the near-infrared fluorescent probe for selectively sensing human cytochrome P450 2J2. *J. Am. Chem. Soc.* **2019**, *141*, 1126−1134.
(77) Zeng, Z.; Zhang, C.; Li, J.; Cui, D.; Jiang, Y.; Pu, K. Activatable polymer nanoenzymes for photodynamic immunometabolic cancer therapy. *Adv. Mater.* **2021**, *33*, 2007247.
(78) Li, H.; Yao, Q.; Xu, F.; Li, Y.; Kim, D.; Chung, J.; Baek, G.; Wu, X.; Hillman, P. F.; Lee, E. Y.; Ge, H.; Fan, J.; Wang, J.; Nam, S. J.; Peng, X.; Yoon, J. An activatable AIEgen probe for high-fidelity monitoring of overexpressed tumor enzyme activity and its application to surgical tumor excision. *Angew. Chem., Int. Ed.* **2020**, *59*, 10186−10195.
(79) Zhou, Q.; Shao, S.; Wang, J.; Xu, C.; Xiang, J.; Piao, Y.; Zhou, Z.; Yu, Q.; Tang, J.; Liu, X.; Gan, Z.; Mo, R.; Gu, Z.; Shen, Y. Enzyme-activatable polymer-drug conjugate augments tumour penetration and treatment efficacy. *Nat. Nanotechnol.* **2019**, *14*, 799−809.

https://doi.org/10.1021/jacsau.1c00553
JACS Au 2022, 2, 246−257